Plasmon-modulated photoluminescence from gold nanostructures and its dependence on plasmon resonance, excitation energy, and band structure

Loan Le Thi Ngoc,[1] Justyna Wiedemair,[1] Albert van den Berg,[1] and Edwin T. Carlen[1,2*]

[1] *MESA + Institute for Nanotechnology, University of Twente, Enschede, The Netherlands*
[2]*Graduate School of Pure and Applied Sciences, University of Tsukuba, Tsukuba, Japan*
[*]*ecarlen@ims.tsukuba.ac.jp*

Abstract: Two distinct single-photon plasmon-modulated photoluminescence processes are generated from nanostructured gold surfaces by tuning the spectral overlap of the incident laser source, localized surface plasmon resonance band, and the interband transitions between the *d* and *sp* bands, near the *X*- and *L*-symmetry points of the electronic band structure of gold. In the main section of the article, the characteristics of these photoluminescence processes are described and discussed. In the last section, the background continuum accompanying surface-enhanced Raman scattering (SERS) spectra from benzenethiol and 4-mercaptopyridine self-assembled monolayers chemisorbed on nanostructured gold surfaces is shown to originate from plasmon-modulated photoluminescence.

OCIS codes: (250.5403) Plasmonics; (160.3900) Metals; (250.5230) Photoluminescence; (240.6695) Surface-enhanced Raman scattering.

References and links

1. A. Mooradian, "Photoluminescence of metals," Phys. Rev. Lett. **22**(5), 185–187 (1969).
2. C. K. Chen, T. F. Heinz, D. Ricard, and Y. R. Shen, "Surface-enhanced second-harmonic generation and Raman scattering," Phys. Rev. B **27**(4), 1965–1979 (1983).
3. M. Moskovits, "Surface enhanced spectroscopy," Rev. Mod. Phys. **57**(3), 783–826 (1985).
4. G. T. Boyd, Z. H. Yu, and Y. R. Shen, "Photoinduced luminescence from the noble metals and its enhancement on rough surfaces," Phys. Rev. B **33**(12), 7923–7936 (1986).
5. P. Apell, R. Monreal, and S. Lundqvist, "Photoluminesence of noble metals," Phys. Scr. **38**(2), 174–179 (1988).
6. T. V. Shahbazyan, "Theory of plasmon-enhanced metal photoluminescence," Nano Lett. **13**(1), 194–198 (2013).
7. M. Guerrisi, R. Rosei, and P. Winsemius, "Splitting of the interband absorption edge in Au," Phys. Rev. B **12**(2), 557–563 (1975).
8. M. R. Beversluis, A. Bouhelier, and L. Novotny, "Continuum generation from single gold nanostructure through near-field mediated intraband transitions," Phys. Rev. B **68**(11), 115433 (2003).
9. J. C. Slater, "Wave functions in a periodic potential," Phys. Rev. **51**(10), 846–851 (1937).
10. A. B. Pippard, "Experimental determination of the Fermi surface in copper," Philos. Trans. R. Soc. Lond. A **250**(979), 325–357 (1957).
11. B. Segall, "Fermi surface and energy bands of copper," Phys. Rev. **125**(1), 109–122 (1962).
12. H. Ehrenreich and H. R. Philipp, "Optical properties of Ag and Cu," Phys. Rev. **128**(4), 1622–1629 (1962).
13. G. A. Burdick, "Energy band structure of copper," Phys. Rev. **129**(1), 138–150 (1963).
14. D. Shoenberg, "The Fermi surfaces of copper, silver and gold I. The de Haas-van Alphen effect," Phil. Trans. R. Soc. A **255**(1052), 85–133 (1962).
15. D. Beaglehole, "The optical properties of the noble metals," Proc. Phys. Soc. **87**(2), 461–471 (1966).
16. N. F. Mott and H. Jones, *The Theory of the Properties of Metals and Alloys* (Clarendon Press, 1936).
17. N. E. Christensen and S. O. Seraphin, "Relativistic band calculation and the optical properties of gold," Phys. Rev. B **4**(10), 3321–3344 (1971).
18. D. E. Aspnes, E. Kinsbron, and D. D. Bacon, "Optical properties of Au: sample effects," Phys. Rev. B **21**(8), 3290–3299 (1980).
19. R. Lässer, N. V. Smith, and R. L. Benbow, "Empirical band calculations of the optical properties of d-band metals. I. Cu, Ag, and Au," Phys. Rev. B **24**(4), 1895–1909 (1981).

#231346 - $15.00 USD Received 2 Jan 2015; revised 9 Feb 2015; accepted 10 Feb 2015; published 23 Feb 2015

20. A. D. Rakic, A. B. Djurisic, J. M. Elazar, and M. L. Majewski, "Optical properties of metallic films for vertical-cavity optoelectronic devices," Appl. Opt. **37**(22), 5271–5283 (1998).
21. P. G. Etchegoin, E. C. Le Ru, and M. Meyer, "An analytic model for the optical properties of gold," J. Chem. Phys. **125**(16), 164705 (2006).
22. A. Tcherniak, S. Dominguez-Medina, W.-S. Chang, P. Swanglap, L. S. Slaughter, C. F. Landes, and S. Link, "One-photon plasmon luminescence and its application to correlation spectroscopy as a probe for rotational and translational dynamics of gold nanorods," J. Phys. Chem. C **115**(32), 15938–15949 (2011).
23. M.-L. Thèye, "Investigation of the optical properties of Au by the means of thin semitransparent films," Phys. Rev. B **2**(8), 3060–3078 (1970).
24. P. B. Johnson and R. W. Christy, "Optical constants of the noble metals," Phys. Rev. B **6**(12), 4370–4379 (1972).
25. A. H. Wilson, *The Theory of Metals* (Cambridge University Press, 1936).
26. R. Leng, J. Opsal, H. Chu, M. Senko, and D. E. Aspnes, "Analytic representations of the dielectric functions of materials for device and structural modeling," Thin Solid Films **132**, 313–314 (1998).
27. K. Imura, T. Nagahara, and H. Okamoto, "Plasmon mode imaging of single gold nanorods," J. Am. Chem. Soc. **126**(40), 12730–12731 (2004).
28. Y. Fang, W.-S. Chang, B. Willingham, P. Swanglap, S. Dominguez-Medina, and S. Link, "Plasmon emission quantum yield of single gold nanorods as a function of aspect ratio," ACS Nano **6**(8), 7177–7184 (2012).
29. J. P. Wilcoxon, J. E. Martin, F. Parsapour, B. Wiedenman, and D. F. Kelley, "Photoluminescence from nanosize gold clusters," J. Chem. Phys. **108**(21), 9137–9143 (1998).
30. M. B. Mohamed, V. Volkov, S. Link, and M. A. El-Sayed, "The 'lightning' gold nanorods: fluorescence enhancement of over a million compared to the gold metal," Chem. Phys. Lett. **317**(6), 517–523 (2000).
31. E. Dulkeith, T. Niedereichholz, T. A. Klar, J. Feldmann, G. von Plessen, D. I. Gittins, K. S. Mayya, and F. Caruso, "Plasmon emission in photoexcited gold nanoparticles," Phys. Rev. B **70**(20), 205424 (2004).
32. T. Shahbazyan, I. E. Perakis, and J.-Y. Bigot, "Size-dependent surface plasmon dynamics in metal nanoparticles," Phys. Rev. Lett. **81**(15), 3120–3123 (1998).
33. M. Yorulmaz, S. Khatua, P. Zijlstra, A. Gaiduk, and M. Orrit, "Luminescence quantum yield of single gold nanorods," Nano Lett. **12**(8), 4385–4391 (2012).
34. H. Hu, H. Duan, J. K. Yang, and Z. X. Shen, "Plasmon-modulated photoluminescence of individual gold nanostructures," ACS Nano **6**(11), 10147–10155 (2012).
35. F. Wackenhut, A. V. Failla, and A. J. Meixner, "Multicolor microscopy and spectroscopy reveals the physics of the one-photon luminescence in gold nanorods," J. Phys. Chem. C **117**(34), 17870–17877 (2013).
36. L. Le Thi Ngoc, M. Jin, J. Wiedemair, A. van den Berg, and E. T. Carlen, "Large area metal nanowire arrays with tunable sub-20 nm nanogaps," ACS Nano **7**(6), 5223–5234 (2013).
37. J. Wiedemair, L. Le Thi Ngoc, A. van den Berg, and E. T. Carlen, "Surface-enhanced Raman spectroscopy of self-assembled monolayer conformation and spatial uniformity on silver surfaces," J. Phys. Chem. C **118**(22), 11857–11868 (2014).
38. M. Jin, H. van Wolferen, H. Wormeester, A. van den Berg, and E. T. Carlen, "Large-area nanogap plasmon resonator arrays for plasmonics applications," Nanoscale **4**(15), 4712–4718 (2012).
39. L. Le Thi Ngoc, T. Yuan, M. Odijk, A. van den Berg, H. Permentier, R. Bischoff, and E. T. Carlen, "Surface-enhanced Raman spectroelectrochemical analysis system with metalloporphyrin modified electrodes for drug metabolism investigation," *in Proceedings of the International Conference on Raman Spectroscopy* (2014).
40. T. E. Furtak and J. A. Reyes, "Critical analysis of theoretical models for the giant Raman effect from adsorbed molecules," Surf. Sci. **93**(2-3), 351–382 (1980).
41. M. Moskovits, "Surface-enhanced Raman spectroscopy: a brief perspective," J. Raman Spectrosc. **36**(6-7), 485–496 (2005).
42. J. I. Gersten, R. L. Birke, and J. R. Lombardi, "Theory of enhanced light scattering from molecules adsorbed at the metal-solution interface," Phys. Rev. Lett. **43**(2), 147–150 (1979).
43. E. Burstein, Y. J. Chen, C. Y. Chen, S. Lindquist, and E. Tosatti, "Giant Raman scattering by adsorbed molecules on metal surfaces," Solid State Commun. **29**(8), 567–570 (1979).
44. H. Seki and T. J. Chuang, "The role of cavity sites in surface-enhanced Raman scattering," Chem. Phys. Lett. **100**(5), 393–396 (1983).
45. S. Mahajan, R. M. Cole, J. D. Speed, S. H. Pelfrey, A. E. Russell, P. N. Bartlett, S. M. Barnett, and J. J. Baumberg, "Understanding the surface-enhanced Raman spectroscopy 'background'," J. Phys. Chem. C **114**(16), 7242–7250 (2010).
46. J. P. Heritage, J. G. Bergman, A. Pinczuk, and J. M. Worlock, "Surface picosecond Raman gain spectroscopy of a cyanide monolayer on silver," Chem. Phys. Lett. **67**(2-3), 229–232 (1979).
47. R. L. Birke, J. R. Lombardi, and J. I. Gersten, "Observation of a continuum in enhanced Raman scattering from a metal-solution interface," Phys. Rev. Lett. **43**(1), 71–75 (1979).
48. A. Otto, "Raman scattering from adsorbates on silver," Surf. Sci. **92**(1), 145–152 (1980).
49. A. M. Michaels, J. Jiang, and L. Brus, "Ag nanocrystal junctions as the site for surface-enhanced Raman scattering of single rhodamine 6G molecules," J. Phys. Chem. B **104**(50), 11965–11971 (2000).
50. T. Itoh, V. Biju, M. Ishikawa, Y. Kikkawa, K. Hashimoto, A. Ikehata, and Y. Ozaki, "Surface-enhanced resonance Raman scattering and background light emission coupled with plasmon of single Ag nanoaggregates," J. Chem. Phys. **124**(13), 134708 (2006).

#231346 - $15.00 USD Received 2 Jan 2015; revised 9 Feb 2015; accepted 10 Feb 2015; published 23 Feb 2015

51. H. Ueba, "Effective resonant light scattering from adsorbed molecules," J. Chem. Phys. **73**(2), 725–732 (1980).
52. G. Varsanyi, *Vibrational Spectra of Benzene Derivates* (Academic Press, 1969).
53. M. E. Abdelsalam, P. N. Bartlett, J. J. Baumberg, S. Cintra, T. A. Kelf, and A. E. Russell, "Electrochemical SERS at a structured gold surface," Electrochem. Commun. **7**(7), 740–744 (2005).

1. Introduction

Photoluminescence from thin films of copper and gold was first reported forty-five years ago, and was attributed to the direct recombination of photoexcited *sp*-conduction band electrons with *d*-band holes that were scattered to momentum states less than Fermi momentum [1]. Many years later the discoveries of surface-enhanced Raman scattering (SERS) and second harmonic generation (SHG) on roughened noble metal surfaces stimulated further investigation of single-photon and multi-photon metal photoluminescence [2–4]. Boyd and associates conducted a series of single-photon and multiphoton experiments on smooth and roughened surfaces of silver, copper, and gold [4], where photoluminescence peaks were assigned to interband transitions near the *X*- and *L*-symmetry points in the electronic band structure. Furthermore, they reported that roughened surfaces increase the photoluminescence absorption and emission efficiencies through the enhancement of local optical fields by a localized surface plasmon resonance. The photoluminescence process in noble metals has been described as a three-step process consisting of *d*-hole: i) Photoexcitation (quantum efficiency, q_E), ii) Relaxation (quantum efficiency, q_R), and iii) Recombination (quantum efficiency, q_D) due to interband transitions near the *X*- and *L*-symmetry points [4,5]. In the first step, electrons are induced into the *sp*-band by incident radiation, and holes into the *d*-band, thus establishing non-equilibrium populations of electrons and holes. The photoexcited populations are subsequently subjected to a thermalization process consisting of electron-electron and electron-phonon scattering processes, which results in very fast energy and momentum relaxation. In the final step, a small fraction of *d*-band holes, with momentum less than the Fermi momentum, recombine radiatively with *sp*-band electrons via vertical momentum space transitions [4,5]. The total quantum efficiency of the photoluminescence process can be expressed as a combination of the quantum efficiency of each process, $Q_E = q_E q_R q_D$ [4–6]. In conventional metal photoluminescence, q_R and q_D are dominated by fast non-radiative relaxation processes, thus resulting in very low Q_E [4,6].

In the visible spectrum, gold photoluminescence primarily originates from 5*d*-6*sp* interband transitions near the *X*- and *L*-symmetry points in the electronic band structure. The energy band (*E*-*k*) diagrams of the partial electronic band structure of gold in the first Brillouin zone are shown in Figs. 1(a) and 1(b) [7]. The interband transitions Δ_X and Δ_L are shown near the *X*- and *L*-symmetry points, respectively, where the 5*d* bands are relatively flat. A critical point is defined as the energy where $dE(k)/dk = 0$ of two bands, hence are parallel, which corresponds to a van Hove singularity in the joint density of electron states. When the bands are not parallel, i.e. $dE(k)/dk \neq 0$, the joint density of states will be reduced, however, the absorption rate due to interband transitions can be significant, especially when one of the bands is relatively flat, as is the case of the 5*d* bands near the *X*- and *L*-symmetry points shown in Fig. 1. It should be noted that photoluminescence due to intraband transitions is also possible, which involves electron-hole pairs generated in the *sp*-band by near-infrared excitation energies, but is typically much weaker than photoluminescence due to interband transitions [8]. Research to discover the electronic band structure of noble metals dates back over seventy-five years to work on copper [9–13], where energy band structures and Fermi surfaces were first constructed. Similar to copper, gold has a face centered cubic crystal structure with a distorted spherical free electron Fermi surface that touches the first Brillouin zone on the hexagonal faces of the crystal, thus producing *neck* and *belly* regions called the *L*-symmetry and *X*-symmetry points, respectively [14]. Beaglehole developed an energy band structure of gold and identified a high density of states in the first Brillouin zone near the *X*-

#231346 - $15.00 USD Received 2 Jan 2015; revised 9 Feb 2015; accepted 10 Feb 2015; published 23 Feb 2015

and *L*-symmetry points, where the *d*-bands are relatively flat in momentum space, as shown in Fig. 1 [15].

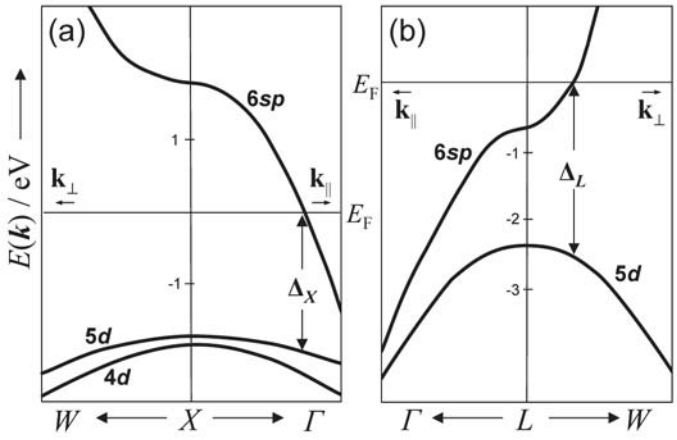

Fig. 1. Select symmetry regions of the first Brillouin zone of the energy band $E(\boldsymbol{k})$ diagram of gold. (a) *X*-symmetry point and interband transition Δ_X. (b) *L*-symmetry point and interband transition Δ_L. The electron wave vector $\boldsymbol{k}_\parallel$ points from the *X*- and *L*-symmetry points to the *Γ*-symmetry point, and $\boldsymbol{k}_\perp$ point in the direction of the *W*-symmetry point [7].

It is now well established that the *d*-band density of states is larger and more strongly localized near the symmetry points compared to the *sp*-band, which have a more broad distribution of allowed energy states [7,16,17]. Geurrisi and associates were the first to observe that the optical absorption of gold in the visible spectrum is split between two interband transitions, one located near the *X*-symmetry point with $\Delta_X \approx 1.94$ eV, shown in Fig. 1(a), and the other near the *L*-symmetry point with $\Delta_L \approx 2.45$ eV shown in Fig. 1(b) [7]. The interband transition energy near the *X*-symmetry point was later reported to be $\Delta_X \approx 1.84 \pm 0.02$ eV, after correcting for intraband absorption [18,19]. In single-photon experiments, Boyd, et al. assigned photoluminescence peaks near 2.4 eV to the 5*d*-6*sp* interband transition Δ_L, 2.2 eV to the combination of the 5*d*-6*sp* interband transition Δ_L and the 4*d*-6*sp* interband transition, and 1.9 eV to the 5*d*-6*sp* interband transitions Δ_X. For the excitation energies considered in this article ($\hbar\omega_{01} = 1.96$ eV and $\hbar\omega_{02} = 2.33$ eV), which are commonly used for plasmonics applications, the Δ_X interband transition of the 5*d* and 6*sp* bands is the most important for the plasmon-enhanced optical response of gold [4,19]. Although the selection rules for conventional dipole transitions between the *d*-band and *sp*-band states are forbidden, the large *d*-band density of electron states near the *X*-symmetry point compensates the small transition matrix elements, from Fermi's golden rule. For plasmon-modulated interband transitions, the conventional selection rules for dipole processes may not strictly hold due to the strongly confined fields with large field gradients [8].

The optical response of gold, as well as the other noble metals, is characterized by interband absorption due to the fact that incident electromagnetic fields can penetrate into the surface of gold, hence increasing the probability of interband transitions. Despite extensive work to understand the electronic band structure of gold and the details of the interband absorption near the *X*- and *L*-symmetry points [7], very often only the interband transition near Δ_L is referred to when describing the optical absorption of gold [20–22]. This is reasonable in many cases considering the fact that the absorption cross-section near Δ_X is much weaker than Δ_L [4,7,23,24]. The optical response of gold is described by the dielectric function, which is typically represented by the generic spectral model [25]

#231346 - $15.00 USD Received 2 Jan 2015; revised 9 Feb 2015; accepted 10 Feb 2015; published 23 Feb 2015

$$\varepsilon(\omega) = \omega_\infty - \frac{\omega_p^2}{\omega^2 i\gamma_p \omega} + \chi_X(\omega) + \chi_L(\omega), \tag{1}$$

where ε_∞ is a constant term representing the ion-core contribution at long wavelengths, ω_p and γ_p are the plasma frequency and electron damping rate, respectively, and $\chi_i(\omega)$ are susceptibility functions that represent the optical absorption of each interband transition

$$\chi_{X,L}(\omega) = A_{X,L}[e^{i\theta}(\omega_{X,L} - \omega - i\gamma_{X,L})^{-1} + e^{-i\theta}(\omega_{X,L} + \omega + i\gamma_{X,L})^{-1}], \tag{2}$$

where A_i is the amplitude, $\hbar\omega_i \equiv \Delta_i$ is the interband transition energy, γ_i = are the loss parameters, and θ a phase term [26]. The dielectric function can be factored into real and imaginary components $\varepsilon(\omega) = \varepsilon_1(\omega) + i\varepsilon_2(\omega)$, where $\varepsilon_2(\omega)$ represents the interband transitions. Figure 2 shows measured $\varepsilon_1(\omega)$ and $\varepsilon_2(\omega)$ data from Thèye (solid red circles) [23] and Johnson and Christy (solid blue triangles) [24], and the solid black traces are generated from the analytical model, Eq. (1) and Eq. (2), with $\hbar\omega_X \equiv \Delta_X = 1.84$ eV and $\hbar\omega_L \equiv \Delta_L = 2.45$ eV, $\varepsilon_\infty = 1.5$, $\omega_p = 1.37 \times 10^{16}$ s^{-1}, $\theta = -\pi/2.7$, $A_X = 0.4 \times 10^{15}$, $\gamma_X = 1.2 \times 10^{15}$ s^{-1}, $A_L = 0.95 \times 10^{16}$, $\gamma_L = 1.4 \times 10^{15}$ s^{-1}. The excitation energies, $\hbar\omega_{01}$ and $\hbar\omega_{02}$, used in this article are shown with red and green dashed lines, respectively. It has been previously established that interband transitions near Δ_X have broad absorption profiles, in contrast to the absorption profile near Δ_L, both of which are not clearly represented in the experimental data of gold [23,24].

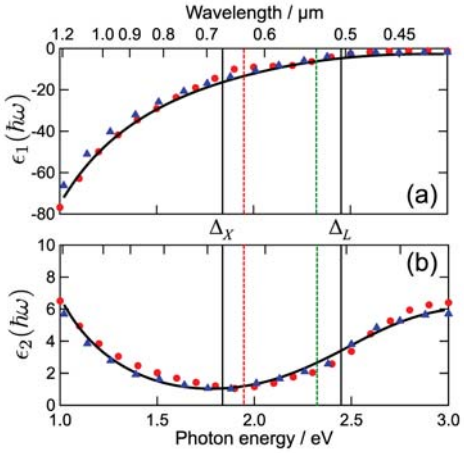

Fig. 2. (a) Real and (b) Imaginary dielectric function data from gold thin films. Red solid circles [23], blue solid triangles [24], and black line from analytical model. The solid vertical lines indicate Δ_X and Δ_L. The dashed lines indicate the excitation energies $\hbar\omega_{01} = 1.96$ eV (red) and $\hbar\omega_{02} = 2.33$ eV (green).

The absorption does increase for photon energies above Δ_L. The absorption increase for photon energies below approximately 1.5 eV is due to the free-electron behavior of gold. When plasmon-modulated photoluminescence is combined with moderate-power laser sources with emission energies located between Δ_X and Δ_L, the *X*-symmetry point dominates the photoluminescence response, which will be described in subsequent sections [27]. Furthermore, for excitation energies in the near-infrared, intraband transitions can produce photoluminescence, which can also be plasmon-modulated in gold nanostructures [8,28].

There have been many reports of single-photon induced plasmon-modulated photoluminescence from gold nanostructures. Boyd and associates described plasmon-modulated photoluminescence intensity, due to the enhancement of the radiative decay rate of the localized *d*-hole and *sp*-electron recombination dipole, as $I_{PL} \sim [L(\omega_0)]^2[L(\omega_{PL})]^2$, where L is a local field factor that accounts for the enhancement of the excitation and emission fields

#231346 - $15.00 USD Received 2 Jan 2015; revised 9 Feb 2015; accepted 10 Feb 2015; published 23 Feb 2015

crossing the metal interface [4]. In this case, the excitation quantum efficiency q_E, and the recombination quantum efficiency q_D, are both enhanced with respect to their spectral overlap with the surface plasmon band. An early report of plasmon-modulated photoluminescence from small spherical gold colloids excited with ultraviolet radiation (5.39 eV) indicated that Q_E was enhanced by several orders of magnitude with peak emission energy of 2.82 eV [29]. The photoluminescence was attributed to the radiative recombination of 5*d*-6*sp* electron-hole pairs. Mohamed and associates reported photo-luminescence measurements from gold nanorod assemblies with varying aspect ratios using an excitation energy of 2.6 eV [30]. Peaks in the aspect ratio dependent scattering spectra directly corresponded to the plasmon-modulated photoluminescence peaks, and it was concluded that the longitudinal surface plasmon resonance is more efficient at enhancing the photoluminescence intensity, thus both the incoming excitation and the outgoing emitted radiation are enhanced, as previously reported [4]. Dulkeith and associates later reported plasmon-modulated photoluminescence from spherical gold nanoparticles using a 3.3 eV excitation source [31]. The reported Q_E was enhanced by several orders of magnitude, and the peak of the photoluminescence band corresponded directly to the peak of the localized surface plasmon resonance scattering spectra, which varied from 2.3 to 2.4 eV. Since the spectral overlap of the excitation source with the peak of the scattering spectra was very weak, the authors argued that the enhancement of q_E and q_D could not account for the large enhancement of Q_E. Additionally, the peak positions of photoluminescence and scattering spectra shift alike, thus preclude the possibility that the photoluminescence spectrum simply reflects the joint density of states of *d*-band holes and *sp*-band electrons. The authors proposed a three-step model based on a previously reported model [32], which consists of a process where photoexcited *d*-band holes relax within the *d*-band, then scatter to the conduction band via emission of surface plasmons, which subsequently decay radiatively. More recently, single-photon photoluminescence from gold nanorods was studied using 2.41 eV and 1.96 eV excitation sources, and nearly perfect spectral overlap of the luminescence and scattering spectra was reported. They reported that the interband transitions and transverse surface plasmons are excited with the 2.41 eV laser source, in contrast to the longitudinal surface plasmon resonance excited by the 1.96 eV laser source, thus was attributed to the fast interconversion between surface plasmons and hot electron pairs, and concluded that the luminescence occurs via emission by the radiative decay of surface plasmons [22]. Yorulmaz, et al. studied single-photon photoluminescence from gold nanorods with different aspect ratios using a 2.6 eV excitation source, and found a strong correlation between the scattering and photoluminescence spectra of the same particle, thus confirming the plasmonic contribution to the measured photoluminescence [33]. They observed that emission was dominated by a polarized contribution that coincides with the longitudinal surface plasmon resonance. In addition to the plasmon-modulated photoluminescence, they observed an additional photoluminescence peak near 2.5 eV that was not affected by the surface plasmon resonance. Hu et al. recently reported a series of experiments from nanopatterned gold disks, and disk-dimers with varying nanogap spacing, using a 2.33 eV excitation source [34]. They observed that the peak photoluminescence emission energy was strongly dependent on the location of the surface plasmon resonance energy, and the peak photoluminescence emission energy was larger, by up to 70 meV, than the peak surface plasmon resonance energy. More recently, gold nanorod photoluminescence was reported to be produced by three different mechanisms, which includes the excitation of longitudinal and transverse surface plasmon modes, an energy transfer mechanism between the transverse and longitudinal plasmon modes, and the direct excitation of longitudinal surface plasmon modes by photoexcited electrons [35]. Currently, two different models are typically used to explain the different plasmon-modulated photoluminescence observations. The first model (model-1) involves a local optical field enhancement of the quantum efficiencies, q_E and q_D, of a single-photon photoluminescence process when $\hbar\omega_{SPR} \sim \hbar\omega_0 \sim \Delta_{X,L}$ [4,6,30]. In this case, the external field polarizes the nanostructure, thus inducing collective

#231346 - $15.00 USD Received 2 Jan 2015; revised 9 Feb 2015; accepted 10 Feb 2015; published 23 Feb 2015

electron oscillations and a localized surface plasmon resonance, which results in a local optical field enhancement. The origin of model-1, where the excitation and emission channels are separately enhanced, was borne from studies of SERS and SHG [2,3]. In the second model (model-2), the highly localized *d*-hole photoexcitation forms a dipole near Δ_X, or Δ_L, that polarizes the nanostructure due to dynamically screened electron-electron interactions induced by the nanostructure confinement, thus establishing a collective free electron oscillation and localized surface plasmon resonance, which can subsequently decay radiatively giving plasmon-modulated photoluminescence [22,31,32,34].

In this article, we investigate conventional photoluminescence, from planar (unpatterned) as-deposited thin films of polycrystalline gold, and plasmon-modulated photoluminescence, from large area nanostructured gold nanogap surfaces. It should be noted that most of the previous reports of plasmon-modulated photoluminescence of gold were based on nanoparticles, however, the high uniformity of the nanostructured gold surfaces used here have tunable and highly reproducible plasmon resonances [36], thus enabling such systematic studies. Using laser excitation energies located between the interband transitions Δ_X and Δ_L, we demonstrate two very different plasmon-modulated photoluminescence processes that are strongly dependent on the spectral overlap of the localized surface plasmon resonance band (with peak energy $\hbar\omega_{SPR}$), the excitation energy $\hbar\omega_0$, and the interband transition $\Delta_X \approx 1.8$ eV. In the last section of the article, we examine the relationship between plasmon-modulated photoluminescence and the background continuum that accompanies the SERS spectra from benzenethiol and 4-mercaptopyridine self-assembled monolayers (SAM) chemisorbed on the nanostructured gold surfaces.

2. Results and discussion

Photoluminescence experiments are done using two different continuous wave (cw) laser sources: helium-neon (He-Ne) with emission energy 1.96 eV, and neodymium-doped yttrium aluminum garnet (Nd-YAG) with emission energy 2.33 eV, which are both commonly used for plasmonics applications. All measurements are done in an ambient air environment at room temperature. Planar (unpatterned) as-deposited gold layers are fabricated by sputtering gold with thickness in the range of 40-100 nm, on silicon nitride (SiN) coated silicon (Si) samples. Nanostructured gold surfaces, previously reported by our research group [36,37], are fabricated by sputter coating gold directly on nanopatterned SiN template surfaces, which results in large area arrays of metal nanowires that are each separated by sub-20 nm nanogaps. Figures 3(a) and 3(b) show scanning electron microscopy (SEM) images of representative nanostructured gold surfaces used for photoluminescence and SERS measurements. The surface plasmon resonance is generated in the nanogap regions using a normally incident excitation source with linear polarization aligned perpendicular to the length of the nanogap (p-polarization state) [36,37]. Figures 4(a)-4(d) show two-dimensional (2D) finite difference time domain (FDTD) numerical simulation results of the electromagnetic fields near the modeled nanostructured gold surface with pitch Λ_g = 200 nm and nanogap spacing g = 10 nm. Figures 4(a) and 4(c) show the gap-mode localized surface plasmon resonance generated in the nanogap regions for p-polarized excitation using 1.96 eV and 2.33 eV excitation energies, respectively. Figures 4(b) and 4(d) show that an s-polarized excitation source does not produce the gap-mode localized surface plasmon resonance and essentially behaves as a planar gold surface. The surface plasmon resonance band (with peak energy $\hbar\omega_{SPR}$) of the nanostructured gold surfaces can be precisely tuned throughout the visible spectrum by changing the nanogap pitch Λ_g and spacing g [36], which is used to investigate the influence of the plasmon resonance on the photoluminescence emission.

#231346 - $15.00 USD Received 2 Jan 2015; revised 9 Feb 2015; accepted 10 Feb 2015; published 23 Feb 2015

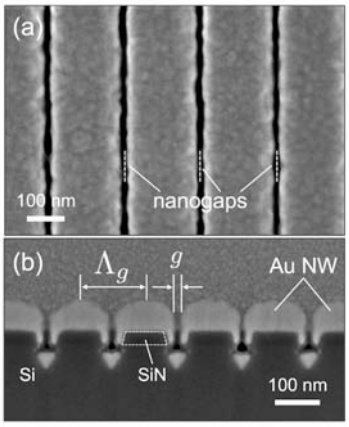

Fig. 3. Representative SEM images of nanostructured gold surfaces with array pitch Λ_g = 200 nm and nanogap spacing g = 10 nm. (a) Top view. (b) Cross-section view.

Figures 4(e) and 4(f) show reflectance spectra calculated using 2D rigorous coupled waveguide analysis (RCWA) code. As the nanogap spacing is reduced from g = 10 nm, shown in Fig. 4(e), to g = 5 nm, shown in Fig. 4(f), the surface plasmon resonance wavelength (the minimum reflectance located at the dip of the reflectance spectrum) from p-polarized excitation red-shifts, which is consistent with our previous reports [36,37].

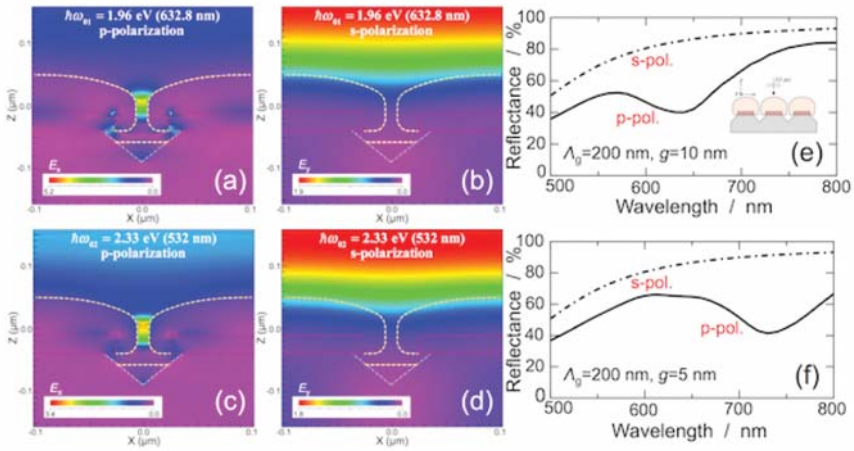

Fig. 4. (a-d) 2D FDTD simulations of electric field profiles near gold nanogaps for different excitation energy and polarization with Λ_g = 200 nm and g = 10 nm. (yellow dashed lines indicate Au layer; red dashed lines indicate SiN layer and gray dashed lines indicate the Si layer). (a) Excitation energy $\hbar\omega_{01}$ = 1.96 eV and p-polarization. (b) $\hbar\omega_{01}$ = 1.96 eV and s-polarization. (c) $\hbar\omega_{02}$ = 2.33 eV and p-polarization. (d) $\hbar\omega_{02}$ = 2.33 eV and s-polarization. (e-f) 2D RCWA simulations of reflectance spectra from gold nanogap surfaces with pitch Λ_g = 200 nm. Solid lines indicate p-polarized reflectance and dashed-dotted lines indicate s-polarized reflectance (e) g = 10 nm. (f) g = 5 nm.

Incident s-polarized excitation does not induce a localized surface plasmon resonance, which is consistent with FDTD simulations and experimental reflectance measurements. In subsequent experiments, the plasmon-enhanced photoluminescence is investigated by varying the nanogap spacing, and thus the localized surface plasmon resonance energy, which is used to investigate the characteristics of plasmon-enhanced photoluminescence from the nanostructured gold surfaces. For subsequent analyses, three metrics are defined to aid in quantifying the spectral overlaps of $\hbar\omega_0$, $\hbar\omega_{SPR}$, and Δ_X. The energy difference of the peak

#231346 - $15.00 USD Received 2 Jan 2015; revised 9 Feb 2015; accepted 10 Feb 2015; published 23 Feb 2015

surface plasmon resonance energy and the excitation energy is indicated as $\delta_E = \hbar (\omega_{SPR}-\omega_0)$. The energy difference of the peak surface plasmon resonance energy and the interband transition energy is $\delta_{SX} = \hbar\omega_{SPR}-\Delta_X$. Small values of δ_E and δ_{SX} indicate strong spectral overlaps.

2.1 He-Ne laser excitation

Photoluminescence spectra generated with a focused cw He-Ne laser source (1.96 eV) of varying laser power levels from planar 100 nm thick gold layers are shown in Fig. 5. The maximum power density of the focused laser source is 0.7 MW cm^{-2} (4 mW power). The photoluminescence from planar gold layers is not dependent on the polarization state of the laser source and the average peak photoluminescence intensity increases linearly with laser power, thus ensuring single-photon absorption. Low laser powers and short integration times are used because we are interested in the plasmon-enhanced photoluminescence responses commonly observed in SERS spectra, and additionally, to avoid sample heating. The peak photoluminescence intensity from planar gold layers is very weak, which is consistent with previous reports of small Q_E for thin gold films [1,4,7]. The peak photoluminescence energy from the planar gold layers is $\hbar\omega_{PL}\approx(1.86 \pm 0.02)$ eV, which correlates well with previously reported values and is consistent with radiative recombination of 5*d*-6*sp* transitions near Δ_X [4,18,19]. The photoluminescence measurements show a tail-like distribution on the low-energy side of the spectrum.

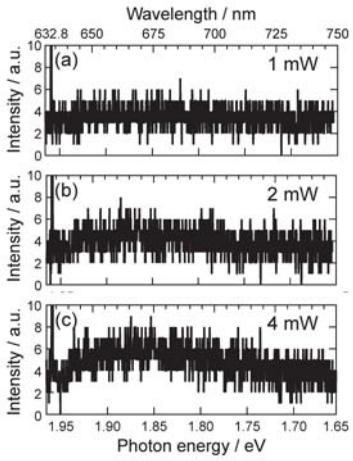

Fig. 5. Representative photoluminescence spectra from planar as-deposited gold layers excited with a He-Ne laser ($\hbar\omega_{01}$ = 1.96 eV) at different power levels. (a) 1 mW. (b) 2 mW. (c) 4 mW. A 100 ms integration time was used for all measurements.

Figure 6 shows representative reflectance and photoluminescence spectra from nanostructured gold surfaces. Different peak surface plasmon resonance bands are shown in the reflectance spectra, where surface S_1 is shown in Fig. 6(a), surface S_2 is shown in Fig. 6(c), and surface S_3 is shown in Fig. 6(e). The surface plasmon resonance band is varied by changing the nanogap spacing *g*, as shown in simulation results of Figs. 4(e) and 4(f). The experimental reflectance spectra are generated using p-polarized white light and the photoluminescence spectra are generated using a p-polarized He-Ne laser. Since the He-Ne laser excitation energy ($\hbar\omega_{01}$ = 1.96 eV) is located on the high-energy side of Δ_X, the plasmon-modulated photoluminescence is due to interband transitions near Δ_X [4,7,19]. The peak photoluminescence energy $\hbar\omega_{PL}$ from all three of the nanostructured surfaces remains approximately constant at ($\hbar\omega_{PL}$ = 1.87 ± 0.01) eV (the peak emission energies were estimated by fitting a polynomial function to the emission bands from *n* = 50 measurements from each surface.) For surface S_1 ($\hbar\omega_{SPR}$ = 2.2 eV), the average emission energy is $\hbar\omega_{PL}$ =

#231346 - $15.00 USD Received 2 Jan 2015; revised 9 Feb 2015; accepted 10 Feb 2015; published 23 Feb 2015

1.87 eV (663 ± 2 nm); for surface S_2 ($\hbar\omega_{SPR}$ = 2.1 eV), the average emission energy is $\hbar\omega_{PL}$ = 1.86 eV (665 ± 3 nm); and for surface S_3 ($\hbar\omega_{SPR}$ = 1.9 eV), the average emission energy is $\hbar\omega_{PL}$ = 1.87 eV (663 ± 2 nm), which are blue-shifted from the peak photoluminescence of the planar gold surfaces by about 10 meV, but more importantly $\hbar\omega_{PL}$ does not shift as the spectral overlap of $\hbar\omega_{SPR}$ with $\hbar\omega_{01}$ is varied, i.e. as δ_E is varied from large (260 meV) to small (−50 meV) values, shown in Figs. 6(b), 6(d), and 6(f). The emission band shape does change as a function of the spectral overlap. The peak photoluminescence intensity is strongly modulated as the spectral overlap is varied.

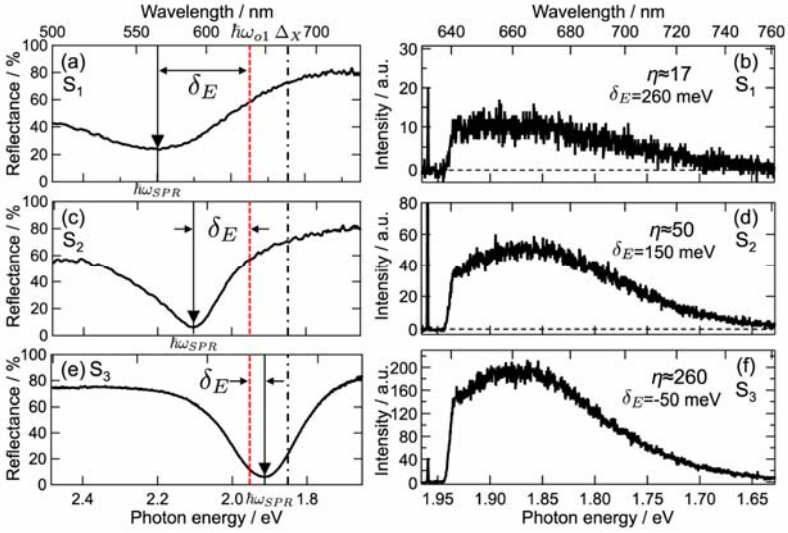

Fig. 6. Representative reflectance and photoluminescence spectra from three different nanostructured gold surfaces (Λ_g = 200 nm and different g) each with different surface plasmon resonance energy $\hbar\omega_{SPR}$. The excitation energy (1.96 eV) is indicated with a dashed red line. The location of the Δ_X interband transition is indicated with a dashed-dotted line. (a),(b) Surface S_1 with δ_E≈260 meV. (c),(d) Surface S_2 with δ_E≈150 meV. (e),(f) Surface S_3 δ_E≈-50 meV. A He-Ne laser excitation source with 1 mW power and 100 ms integration time was used for all measurements. Note the different intensity scales in the photoluminescence plots.

For δ_E≈260 meV (the weakest spectral overlap), the peak photoluminescence intensity is enhanced by a factor of η≈17, where η is defined as the ratio of the peak plasmon-modulated photoluminescence intensity to the photoluminescence intensity measured from a planar gold layer. For δ_E≈150 meV (increased spectral overlap), the photoluminescence is further enhanced to η≈50, shown in Figs. 6(c) and 6(d), and as the spectral overlap is increased, with δ_E≈-50 meV, the photoluminescence enhancement factor is further increased to η≈260. The peak plasmon-modulated photoluminescence enhancement (η≈350) occurs near the excitation laser energy $\hbar\omega_{01}$. This photoluminescence enhancement is of the same order of magnitude as the simulated localized electromagnetic field enhancement generated in the nanogap regions with a p-polarized plane wave ($\hbar\omega_{01}$ = 1.96 eV) shown in Fig. 4(a). Since the photoluminescence emission energy does not shift as δ_E is varied, and the photoluminescence intensity is strongly enhanced for a strong spectral overlap (small δ_E), we conclude that the photoluminescence process, in this case, follows model-1, which is due to radiative recombination of 5*d*-holes with 6*sp*-electrons near Δ_X, and enhanced photoluminescence due to the enhancement of q_E and q_D by a local field enhancement via a localized surface plasmon resonance in the nanogap region [4]. Since the *d*-band holes are strongly localized near the *X*-symmetry point, this process can be considered to be resonantly enhanced dipole radiation.

Figure 7 shows the polarization dependence of the reflectance and photoluminescence spectra generated from the gold nanostructured surfaces. For s-polarized incident light (θ =

#231346 - $15.00 USD Received 2 Jan 2015; revised 9 Feb 2015; accepted 10 Feb 2015; published 23 Feb 2015

0°), the reflectance from the nanostructured surface, shown in Fig. 7(a), does not exhibit a localized surface plasmon resonance in the nanogap regions (i.e. no dip in the reflectance spectrum) and behaves approximately as a planar gold surface, which is consistent with the FDTD simulation results, shown in Figs. 4(b) and 4(d), and the RCWA simulation results, shown in Figs. 4(e) and 4(f). For p-polarized incident light (θ = 90°), the reflectance from the nanostructured surface exhibits a strong localized surface plasmon resonance in the nanogap regions with a large reflectance dip ($\hbar\omega_{SPR}$≈1.92 eV) in the reflectance spectra, which is consistent with the FDTD simulation results, shown in Fig. 4(a).

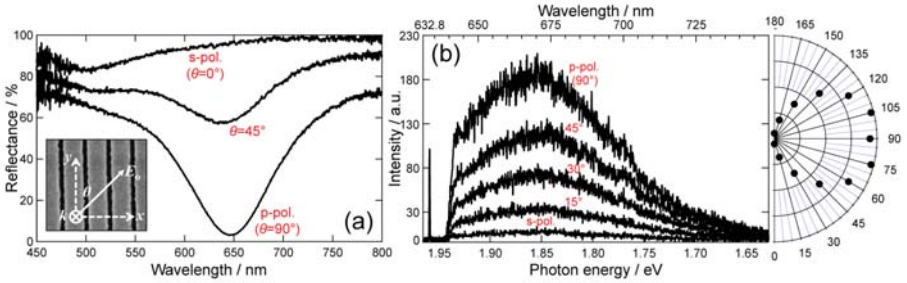

Fig. 7. (a) Reflectance spectra from a representative nanostructured gold surface (Λ_g = 200 nm, g = 10 nm) for different incident light polarizations (p-polarization: electric field polarization perpendicular to the length of the nanogap, and s-polarization: electric field polarization parallel to the length of the nanogap). (b) Photoluminescence spectra as the incident polarization alignment relative to the length of the nanogap structure is varied (inset: laser polarization alignment to nanogap structure). Right: Polar plot of the peak photoluminescence for different polarization alignments.

Figure 7(b) shows photoluminescence spectra from a nanostructured gold surface as the laser excitation (He-Ne, $\hbar\omega_{01}$≈1.96 eV) polarization is varied from a s-polarization state to a p-polarization state. For s-polarized incident excitation, the photoluminescence is very weak, which indicates no plasmon enhancement of the photoluminescence, and is consistent with the experimental reflectance spectra, shown in Fig. 7(a), and simulation results shown in Fig. 4(b). The photoluminescence intensity from the p-polarized excitation is strongly enhanced, which is consistent with the generation of a localized surface plasmon resonance in the nanogap region, as shown in the experimental reflectance spectra, shown in Fig. 7(a), and the simulation results, shown in Figs. 4(a) and 4(e). In this case, $\hbar\omega_{SPR}$≈1.92 eV is located between $\hbar\omega_{PL}$≈1.86 eV and $\hbar\omega_{01}$≈1.96 eV, thus indicating that both channels are strongly enhanced according to model-1, where the photoluminescence intensity is enhanced by a local field enhancement of the excitation (with quantum efficiency q_E) and emission (with efficiency q_D) fields crossing the metal interface as I_{PL}~$[L(\hbar\omega_{01})]^2[L(\hbar\omega_{PL})]^2$ [4]. These measurements, in combination with the simulation results, support the enhancement of Q_E as the mechanism of the plasmon-enhanced photoluminescence for $\hbar\omega_{01}$~$\hbar\omega_{SPR}$~Δ_L.

2.2 Nd-YAG laser excitation

Photoluminescence spectra generated with a focused cw Nd-YAG laser source (2.33 eV) of varying laser power from planar 100 nm thick gold layers are shown in Fig. 8. The maximum power density of the focused laser source is 0.9 MW cm^{-2} (4 mW power). The average peak photoluminescence intensity increases linearly with laser power. The photoluminescence from planar gold layers is not dependent on the polarization state of the laser source and the average peak photoluminescence intensity increases linearly with laser power. The average peak photoluminescence emission energy from planar gold thin films is $\hbar\omega_{PL}$≈2.24 eV, and the peak photoluminescence intensity is approximately 20 × greater than the photoluminescence generated by the He-Ne laser source.

#231346 - $15.00 USD Received 2 Jan 2015; revised 9 Feb 2015; accepted 10 Feb 2015; published 23 Feb 2015

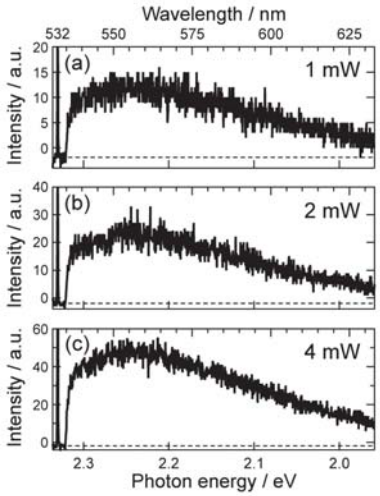

Fig. 8. Photoluminescence spectra from planar gold layers using a Nd-YAG laser source (2.33 eV) at different power levels. (a) 1 mW. (b) 2 mW. (c) 4 mW. Note the different intensity scales. A 100 ms integration time was used for all measurements.

Since the 2.33 eV excitation energy is lower than Δ_L, shown in Fig. 1(b), interband transitions near Δ_L are not expected to contribute to the photoluminescence. However, previously reported photoluminescence spectra produced with a similar excitation energy from planar gold surfaces showed a photoluminescence emission energy near 2.2 eV, which was attributed to interband transitions near Δ_L [4]. The same authors reported a peak photoluminescence energy at 2.2 eV, produced with a much larger excitation energy (4.67 eV), and assigned the emission to a combination of 5*d*-6*sp* transitions near Δ_L and 4*d*-6*sp* transitions near Δ_X [4]. However it is not likely that the 4*d*-6*sp* transitions near Δ_X contribute to the photoluminescence in our experiments. The contribution of the Δ_X and Δ_L interband transitions to the photoluminescence generated with the Nd-YAG laser source becomes more evident from the measurements of nanostructured gold surfaces, where the photoluminescence emission characteristics are significantly modified depending on the spectral overlap of $\hbar\omega_0$, $\hbar\omega_{SPR}$, and Δ_X.

Figure 9 shows representative reflectance and photoluminescence spectra from nanostructured gold surfaces with different $\hbar\omega_{SPR}$. For all three surfaces, the spectral overlap of the excitation source and surface plasmon band is very weak with $\delta_E \approx -410$ meV for surface S_1, shown in Fig. 9(a), $\delta_E \approx -280$ meV for S_2, shown in Fig. 9(c), and $\delta_E \approx -650$ meV for S_3, shown in Fig. 9(e), and therefore, we do not expect that the external field can induce a strong surface plasmon resonance, thus q_E is not significantly enhanced [31]. Despite the weak spectral overlap of $\hbar\omega_{02}$, with $\hbar\omega_{SPR}$, the peak photoluminescence intensity and emission energy are significantly modified. For surface S_1, the peak surface plasmon resonance energy is $\hbar\omega_{SPR} \approx 1.92$ eV, and therefore, $\delta_{SX} \approx 60$ meV, thus there is a strong spectral overlap of $\hbar\omega_{SPR}$ with Δ_X. The p-polarized excitation results in a peak photoluminescence emission of $\hbar\omega_{PL,p} \approx 1.98$ eV that is blue shifted from $\hbar\omega_{SPR}$ by about 60 meV. The peak intensity is enhanced by a factor of $\eta_p \approx 2$, compared to the planar gold surfaces. The peak photoluminescence intensity and emission energy ($\hbar\omega_{PL,s} \approx 2.2$ eV) generated with the s-polarized excitation are similar to the conventional photoluminescence from a planar gold surface, which is supported by the FDTD simulation results shown in Fig. 4(d). For surface S_2, $\hbar\omega_{SPR} \approx 2.05$ eV and $\delta_{SX} \approx 190$ meV, thus the spectral overlap of $\hbar\omega_{SPR}$ with Δ_X is reduced. The peak photoluminescence intensity generated with the s-polarized excitation is not enhanced and the peak emission energy is $\hbar\omega_{PL,s} \approx 2.2$ eV, thus similar to the photoluminescence characteristics of a planar gold surface, which is also consistent with the

#231346 - $15.00 USD Received 2 Jan 2015; revised 9 Feb 2015; accepted 10 Feb 2015; published 23 Feb 2015

FDTD simulation results shown in Fig. 4(d). The p-polarized excitation results in a peak photoluminescence emission energy of $\hbar\omega_{PL,p}$≈2.08 eV, which is blue shifted from $\hbar\omega_{SPR}$ by about 30 meV. The peak intensity is enhanced by a factor of η_p≈3. The photoluminescence spectra from surface S_1 and S_2, shown in Figs. 9(a)-9(d), are similar to those reported by Hu, et al. [34], however, our interpretation of the mechanism is slightly different. When the peak surface plasmon resonance energy $\hbar\omega_{SPR}$ is located between Δ_X and Δ_L, and is varied, the resulting peak photoluminescence energy directly correlates with the movement of $\hbar\omega_{SPR}$ accompanied by a small blue shift. In these cases, model-2 is plausible, which is based on the localized dipole near Δ_X polarizing the nanostructure, thus exciting the emission of surface plasmons that subsequently decay radiatively near $\hbar\omega_{SPR}$ [31,32]. Additionally, the shape of the photoluminescence spectrum from surface S_2 with p-polarized excitation is drastically different compared to the other spectra. The total photoluminescence in this case may be due to emission by surface plasmons due to the localized dipole at Δ_X, as well as emission from radiative recombination near Δ_L (≈2.2 eV), which is possible because the surface plasmon resonance band is centrally located and partially overlaps both interband transitions. Dual photoluminescence emission peaks from gold nanorods have been previously reported [33]. For surface S_3, $\hbar\omega_{SPR}$ = 1.68 eV, δ_{SX}≈-180, thus the spectral overlap of $\hbar\omega_{SPR}$ with Δ_X is shifted to the low energy side of Δ_X. With the weak spectral overlap of $\hbar\omega_{SPR}$ with Δ_X, the peak photoluminescence emission shifts back to $\hbar\omega_{PL,p}$≈2.2 eV, which is similar to emission from planar gold surfaces. Since the spectral overlap of the excitation source and the surface plasmon band is very weak (large δ_E), q_E will not be enhanced. The photoluminescence spectra generated with the s-polarized excitation is also similar to that from the planar gold surface. In addition, the photoluminescence emission also contains generation from the 5*d*-6*sp* transition near Δ_L, as was measured from the planar gold surfaces, thus accounting for the gradual intensity decrease on the high energy side of the peak intensity, which was also present in previous reports [33,34].

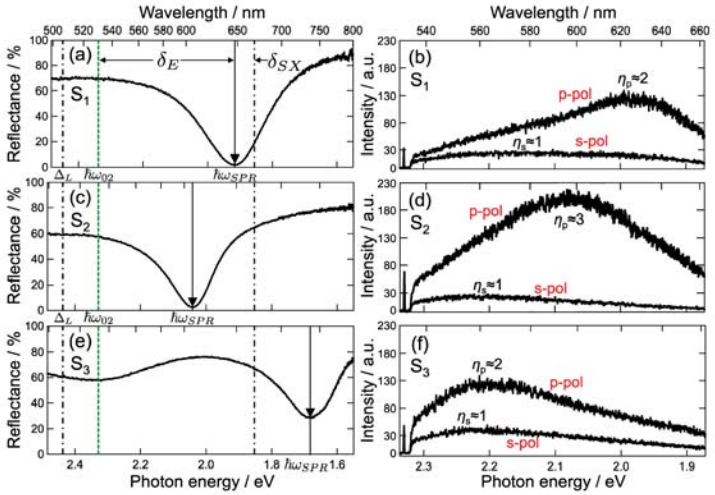

Fig. 9. Reflectance and photoluminescence spectra from three different nanostructured gold surfaces (Λ_g = 200 nm and different *g*) each with different surface plasmon resonance energy $\hbar\omega_{SPR}$. The excitation energy (2.33 eV) is indicated with a dashed green line. The location of the Δ_X and Δ_L interband transitions are indicated with dashed-dotted lines. (a),(b) Surface S_1 with δ_E = –410 meV and δ_{SX}≈60 meV, p-polarized emission peak $\hbar\omega_{PL,p}$≈1.98 eV, and s-polarized emission peak $\hbar\omega_{PL,s}$≈2.2 eV. (c),(d) Surface S_2 with δ_E≈-280 meV and δ_{SX}≈190 meV, p-polarized emission peak $\hbar\omega_{PL,p}$≈2.08 eV, and s-polarized emission peak $\hbar\omega_{PL,s}$≈2.2 eV. (e),(f) Surface S_3 with δ_E≈-650 meV and δ_{SX}≈-180 meV, p-polarized emission peak $\hbar\omega_{PL,p}$≈2.2 eV, and s-polarized emission peak $\hbar\omega_{PL,s}$≈2.2 eV. All measurements conducted with the Nd-YAG laser power of 0.1 mW with 3 s integration time.

#231346 - $15.00 USD Received 2 Jan 2015; revised 9 Feb 2015; accepted 10 Feb 2015; published 23 Feb 2015

2.3 SERS background continuum

Our motivation for studying plasmon-modulated photoluminescence stems from our interest in developing nanostructured noble metal nanostructured surfaces for SERS [36,38], and their application to surface-enhanced Raman spectroscopy [37] and spectroelectrochemistry [39], where all SERS spectra are accompanied by a strong background continuum. The background continuum that accompanies the SERS spectra from molecules adsorbed to metal surfaces has been studied extensively since the discovery of SERS more than forty years ago, and there have been many explanations of the observed phenomena, which have been previously reviewed [3,40,41]. It is important to note that many of the early studies were conducted on silver surfaces using a variety of conditions and adsorbed molecules, and the background continuum accompanying SERS spectra from silver nanostructures is very different compared to the continuum generated on gold nanostructures. Currently, the most commonly accepted models of the background continuum generation mechanism involve the electronic interaction of the surface adsorbed molecules and the free electrons in the metal layer near the interface [42–45]. However, it has been acknowledged that plasmon-modulated photoluminescence from the rough noble-metal films is closely related to SERS and may contribute to the background continuum [3,46]. Other models based on inelastic scattering, adsorbed molecule luminescence, and resonant light scattering have been proposed [46–51]. We show that plasmon-modulated photoluminescence plays a significant role in the SERS background continuum from the gold nanostructured surfaces by directly comparing the photoluminescence spectra from unmodified nanostructured gold surfaces, similar to those presented earlier, to SERS spectra measured from nanostructured gold surfaces modified with benzenethiol and 4-mercaptopyridine SAMs. The photoluminescence and SERS spectra are generated on nanostructured gold surfaces with a focused He-Ne (1.96 eV) laser source.

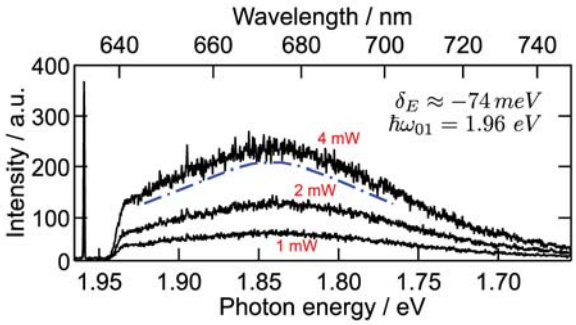

Fig. 10. Photoluminescence spectra from an unmodified nanostructured gold surface (Λ_g = 200 nm, g = 10 nm) excited with a He-Ne laser source. A 100 ms integration time was used for all measurements. Blue dashed-dotted line highlights the general background continuum profile.

Figure 10 shows representative photoluminescence spectra measured from nanostructured gold surfaces fabricated with a strong spectral overlap of $\hbar\omega_{01}$ = 1.96 eV with $\hbar\omega_{SPR}$ (δ_E≈-74 meV). The average peak plasmon-modulated photoluminescence emission energy is $\hbar\omega_{PL}$≈1.84 eV, and the average peak intensity increases linearly with the laser excitation power. The corresponding SERS spectra from the benzenethiol SAM modified nanostructured gold surface is shown in Fig. 11. The Raman vibration bands of benzenethiol chemisorbed on the nanostructured gold surfaces are consistent with previous assignments [52] (the Raman vibration bands of benzenethiol SAM modified nanostructured gold surfaces are 7a(a_1), ν(C-S) + β(C-C-C) (421 cm^{-1}); 6a(a_1), β(C-C-C) + ν(C-S) (696 cm^{-1}); 12(a_1), β(C-C-C) (999 cm^{-1}); 18a(a_1), β(C-H) (1023 cm^{-1}); 1(a_1), β(C-C-C) + ν(C-S) (1072 cm^{-1}); and 8a(a_1), ν(C-C) (1570 cm^{-1})). The vibration band intensities increase linearly with an

#231346 - $15.00 USD Received 2 Jan 2015; revised 9 Feb 2015; accepted 10 Feb 2015; published 23 Feb 2015

increasing laser power as expected. The strong correlation between the plasmon-modulated photoluminescence band shape and the SERS background continuum is evident.

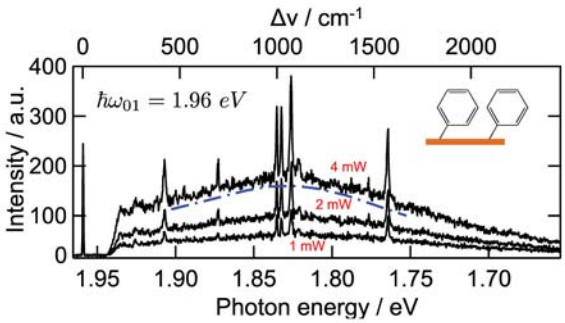

Fig. 11. SERS spectra from a nanostructured gold surface (Λ_g = 200 nm, g = 10 nm) modified with benzenethiol SAM. Raman shift Δν scale located on the top axis. A He-Ne laser source with 100 ms integration time was used for all measurements. Blue dashed-dotted line highlights the general background continuum profile.

Compared to the photoluminescence measurements, shown in Fig. 10, the peak background continuum intensity is reduced by approximately 30%, and the average peak background emission energy is reduced to $\hbar\omega_{PL}$≈1.83 eV. The reduction in the peak photoluminescence intensity in the SERS spectrum can be explained by the fact that the surface plasmon resonance band is red-shifted due to the increased dielectric constant of benzenethiol on the gold surface (ε~2.3) compared to an unmodified gold surface. The increased dielectric constant results in a decreased $\hbar\omega_{SPR}$, thus in a reduced spectral overlap with $\hbar\omega_{01}$ (increased δ_E) and reduction in the peak photoluminescence intensity, as shown in Fig. 6. The shift of the peak emission $\hbar\omega_{PL}$ to a lower energy (~10 meV) can be explained by considering a reduction in photoluminescence energy induced by the increased dielectric constant at the gold surface where the emission energy is determined by the metal interface to the surrounding medium.

Figure 12 shows a SERS spectrum from a nanostructured gold surface modified with a 4-mercaptopyridine SAM. The characteristic vibrations are consistent with previous assignments [52,53] (the Raman vibration bands of 4-mercaptopyridine SAM modified nanostructured gold surfaces are observed at 6a(a_1), ν(C-S) + β(C-C) (700 cm^{-1}); 10b(b_1), ν(C-S) (778 cm^{-1}); 1(a_1), β(C-C-C) (1000 cm^{-1}); 18a(a_1), β(C-H) (1036 cm^{-1}); 12(a_1), β(C-C-C) + ν(C-S) (1094 cm^{-1}); 9a(a_1), β(C-H) (1210 cm^{-1}); 19a(a_1), γ(C = C/C = N) (1274 cm^{-1}); 8b(b_2), γ(C-C) (1577 cm^{-1}) and 8a(a_1), ν(C-C) (1608 cm^{-1})). The average peak background emission energy is also reduced to $\hbar\omega_{PL}$≈1.83 eV, compared to the planar gold surface. It is evident in this case, as well, that the plasmon-modulated photoluminescence for the nanostructured gold surfaces is the primary contributor to the SERS background continuum.

In both cases, the general shape of the background continuum directly corresponds to the plasmon-modulated photoluminescence spectrum when the same excitation source is used, which is indicated with a blue dashed-dotted line, shown in Figs. 10, 11, and 12. Furthermore, the peak intensity of the background continuum increases with increases in the excitation power, or with increases in the plasmon enhancement, consistent with plasmon-modulated photoluminescence.

#231346 - $15.00 USD Received 2 Jan 2015; revised 9 Feb 2015; accepted 10 Feb 2015; published 23 Feb 2015

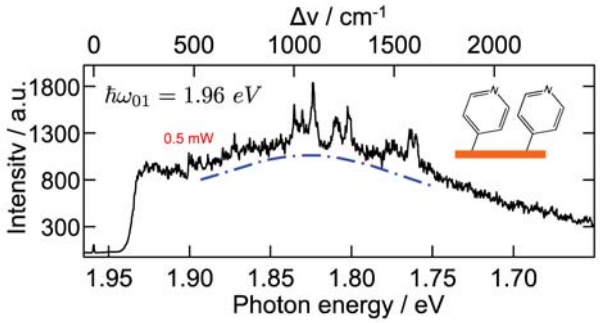

Fig. 12. SERS spectrum from a nanostructured gold surface (Λ_g = 200 nm, g = 10 nm) modified with a 4-mercaptopyridine SAM. Raman shift Δν scale located on the top axis. A He-Ne laser source with 0.5 mW power and 5 s integration time was used for the measurement. Blue dashed-dotted line highlights the general background continuum profile.

These measurements indicate that plasmon-modulated photoluminescence is an important contributor to the SERS background continuum from gold surfaces. Other reports of SERS spectra accompanied by a large background continuum from gold surfaces that contained distinct peaks near 1.85 eV, however, the authors did not report photoluminescence as a source for the background continuum [45,53]. We acknowledge the importance of charge transfer between adsorbed molecules at the surface and the metal layer [42,43,45,49], and we propose that the plasmon-modulated photoluminescence is the primary source of the background continuum and charge transfer between the adsorbed molecule and the gold layer works to modulate the continuum in intensity, emission energy location, and possibly band shape [43,45].

3. Conclusion

In summary, we presented a series of experiments that demonstrate that the plasmon-modulated photoluminescence from gold nanostructures is strongly dependent on the spectral overlap of the surface plasmon resonance energy $\hbar\omega_{SPR}$ with the excitation energy $\hbar\omega_o$ and the interband transition of the 5*d* and 6*sp* bands near the *X*-symmetry point of the electronic band structure. For $\hbar\omega_{01}$(1.96 eV)~Δ_X, the photoluminescence involves 5*d*-6*sp* transitions near Δ_X, and as the spectral overlap of $\hbar\omega_{SPR}$ with $\hbar\omega_{01}$ is varied, the peak photoluminescence emission energy remains approximately constant near Δ_X ($\hbar\omega_{PL}$≈1.87 ± 0.01 eV), while the peak photoluminescence intensity is strongly enhanced relative to the spectral overlap of $\hbar\omega_{01}$ with $\hbar\omega_{SPR}$, i.e. the intensity is strongly enhanced with a strong spectral overlap $\hbar\omega_{01}$~$\hbar\omega_{SPR}$, and weakly enhanced with a weak spectral overlap. When the excitation energy $\hbar\omega_{02}$ (2.33 eV) is located between the interband transitions Δ_X and Δ_L, the resulting photoluminescence involves 5*d*-6*sp* transitions near both interband transitions. As the spectral overlap of $\hbar\omega_{SPR}$ with Δ_X is varied, the peak photoluminescence energy $\hbar\omega_{PL}$ shifts with $\hbar\omega_{SPR}$, which is interpreted as the radiative decay of surface plasmons generated near Δ_X, while the peak photoluminescence intensity is weakly enhanced. For a weak spectral overlap of $\hbar\omega_{SPR}$ with Δ_X, the photoluminescence characteristics resemble that of conventional photoluminescence from a planar gold surface. This leads to the result that the *X*-symmetry point of the electronic band structure, which is largely negligible for conventional gold photoluminescence, is extremely important for plasmon-modulated photoluminescence. Finally, we have shown that the background continuum accompanying SERS spectra, from nanostructured gold surfaces (He-Ne laser source) modified with benzenethiol and 4-mercaptopyridine SAMs, are strongly correlated to plasmon-modulated photoluminescence.

#231346 - $15.00 USD Received 2 Jan 2015; revised 9 Feb 2015; accepted 10 Feb 2015; published 23 Feb 2015

4. Methods

4.1 Nanostructured gold surface fabrication

Conventional silicon (100) substrates have been used for all template fabrication. First, a 30 nm thick low stress silicon nitride (SiN) layer is deposited onto the silicon wafer by low-pressure chemical vapor deposition. A 100 nm polymethyl methacrylate (PMMA, MicroChem Corp.) electron-sensitive photoresist was spin-coated on a silicon substrate and exposed to a 130 pA electron beam with the area dose in the range of 90-120 μAs cm^{-2} (FEI Sirion UHR-SEM). The electron-beam exposure along the length of the SiN template was aligned to the [110] direction of the (100) silicon wafers using the wafer flat as a reference. The total template surface array of 1 mm^2 is written in 100 × 100 μm^2 sections. The exposed regions were developed in a 1:3 methyl isobutyl ketone:isopropanol solution for 30 s, and followed by immersion in isopropyl alcohol. The exposed SiN regions are removed using reactive ion etching (60 W, 25 sccm CHF_3 and 5 sccm O_2) and followed by removal of the remaining PMMA and surface cleaning with oxygen plasma. Prior to silicon etching, the native oxide on the exposed silicon regions was removed by immersion in 1% hydrofluoric acid solution for 1 min. and subsequently rinsed with deionized water. The silicon was etched in a 1% KOH solution at 55 °C with stirring for 45 s and rinsed with deionized water for 2 mins. The different crystal planes etch anisotropically by hydroxide ions in an alkaline solution where (111) planes have the lowest etch rate and (100) and (110) planes both have higher etch rates. The surfaces were then cleaned in a 3:1 piranha solution (H_2SO_4:H_2O_2) for 15 min., rinsed with deionized water for 2 mins., and dried with N_2. The polycrystalline Au layers were sputtered-coated (DC source) in an Ar plasma with a 0.6 nm s^{-1} deposition rate.

4.2 Reflectance measurements

Normal incidence reflection measurements were performed with a p-polarized (LPVISB100, Applied Laser Technology) white light source (100 W tungsten xenon lamp) focused on the Au-NW surfaces with a microscope objective (10 × /0.3 NA, Leica and 100 × /0.9 NA, Olympus). The reflected beam is collected by the same objective and passed through a multimode fiber (QP450-1-XSR, Ocean Optics) to the spectrometer with an integrated detector (HR4000, Ocean Optics). All measurements were calibrated with a planar (unpatterned) as-deposited gold surface on the same template surface with the same nominal metal thickness on the nanostructured metal surface. The polarization dependent reflectance measurements were done by first aligning the sample and rotation stage concentric. The reflectance minimum was then determined by manually rotating the sample a total of 180° from the initial position, in increments of 15°.

4.3 Photoluminescence and Raman scattering measurement instrumentation

A confocal Raman microscope system (alpha300R, Witech GmbH) was used for the Raman scattering and photoluminescence measurements, and is comprised of a TE-cooled charge coupled device (DU970P-BV, Andor Technology, Belfast, Northern Ireland), UHTS300 spectrometer (f/4 300 mm FL; grating: 600 lines mm^{-1}), a fiber coupled confocal configuration with 50 μm core diameter, and fiber coupled laser excitation through a $\lambda/2$ rotator plate for polarization control and laser focusing with the microscope objective. He-Ne (1.96 eV/632.8 nm) and Nd-YAG (2.33 eV/532 nm) laser sources were both used in a backscatter configuration and were focused on the surfaces using a 100 × /NA 0.9 microscope objective (Olympus MPlan FLN). The elastically scattered laser excitation was removed with an edge filter.

4.4 Photoluminescence and Raman scattering measurements

The surface plasmon resonance energy was tuned by controlling the pitch Λ_g and width g of the nanogaps by changing the thickness of the nanostructured gold layer, which is verified

#231346 - $15.00 USD Received 2 Jan 2015; revised 9 Feb 2015; accepted 10 Feb 2015; published 23 Feb 2015

with reflectance measurements. For SERS measurements, the surface plasmon resonance energy was tuned near the laser excitation energy. Benzenethiol and 4-mercaptopyridine self-assembled monolayers were prepared by placing clean nanostructured gold surfaces into a 1 mM ethanol solution for 4 hours. The substrate was gently rinsed with dehydrated ethanol and dried with pure N_2 gas. Raman spectra of benzenethiol and 4-mercaptopyridine SAMs on both planar as-deposited, and nanostructured, gold surfaces have been measured in an ambient air environment. The laser power was measured at the entrance of the microscope objective. The laser sources were focused on the sample surface with 100 × /NA 0.9 microscope objective (Olympus MPlan FLN) with diffraction limited spot diameters ($\phi_s \approx 1.22\lambda_o/NA$) of $\phi_s \approx 860$ nm for the He-Ne laser and $\phi_s \approx 720$ nm for the Nd-YAG laser. The integration time for all Raman spectra is 100 ms unless stated otherwise. Spatial imaging of Raman spectra was performed over 40 × 40 μm^2 areas unless stated otherwise.

4.5 Numerical electromagnetic field simulations

Two-dimensional numerical electromagnetic field simulations were done using FDTD code (Fullwave 6.2, Synopsis, Inc.). Perfectly matched layer boundary conditions have been used at the grid edges, to eliminate reflections. 0.5 nm grid spacing was used for all simulation models. The Brendel-Borman model represents the frequency-dependent dielectric function of gold, which is included in the simulation code. All simulations were checked for proper convergence. Two-dimensional numerical electromagnetic field simulations of the reflectance spectra using a model of the nanostructured gold surface were done using RCWA code (DiffractMOD 3.1, Synopsis, Inc.) using 7 harmonic terms and 0.001 index resolution.

Acknowledgments

The authors thank Jan van Nieuwkasteele and Johan Bomer for helpful comments with device processing, Mark Smithers for assistance with SEM imaging. LLTN thanks the Vietnamese Overseas Scholarship Program (Project number 322) for financial support. Financial support by the Innovative Medicines Initiative (RAPP-ID, Project No. 115153) is gratefully acknowledged.